



HAL
open science

Timescale dependent sign of amorphous titanium dioxide thermo-optic coefficient

Jean-Claude Weeber, Aurore Andrieux, Marie-Maxime Gourier, Juan Arocas, Laurent Markey, Kamal Hammani, Alexandre Bouhelier, Dimitris V Bellas, Elefterios Lidorikis, Nikos Pleros

► To cite this version:

Jean-Claude Weeber, Aurore Andrieux, Marie-Maxime Gourier, Juan Arocas, Laurent Markey, et al.. Timescale dependent sign of amorphous titanium dioxide thermo-optic coefficient. *Optical Materials Express*, 2023, 13 (10), pp.2882-2894. 10.1364/ome.496559 . hal-04287458

HAL Id: hal-04287458

<https://hal.science/hal-04287458>

Submitted on 15 Nov 2023

HAL is a multi-disciplinary open access archive for the deposit and dissemination of scientific research documents, whether they are published or not. The documents may come from teaching and research institutions in France or abroad, or from public or private research centers.

L'archive ouverte pluridisciplinaire **HAL**, est destinée au dépôt et à la diffusion de documents scientifiques de niveau recherche, publiés ou non, émanant des établissements d'enseignement et de recherche français ou étrangers, des laboratoires publics ou privés.



Timescale dependent sign of amorphous titanium dioxide thermo-optic coefficient

JEAN-CLAUDE WEEBER,^{1,*} AURORE ANDRIEUX,¹  MARIE-MAXIME GOURIER,¹ JUAN AROCAS,¹ LAURENT MARKEY,¹ KAMAL HAMMANI,¹  ALEXANDRE BOUHELIER,¹  DIMITRIS V. BELLAS,^{2,3,4} ELEFTERIOS LIDORIKIS,² AND NIKOS PLEROS^{3,4}

¹Laboratoire Interdisciplinaire Carnot de Bourgogne (LICB) UMR 6303, Université de Bourgogne, 9 av. A Savary, BP47870, 21078, Dijon Cedex, France

²Department of Materials Science and Engineering, University of Ioannina, Ioannina, 45110, Greece

³Department of Informatics, Aristotle University of Thessaloniki, Greece

⁴Center for Interdisciplinary Research and Innovation (CIRI-AUTH), Balkan Center, Thessaloniki, 10th km Thessaloniki-Thermi Rd, GR57001, Greece

*jcweeber@u-bourgogne.fr

Abstract: We report on the thermo-optic properties of electron-beam evaporated amorphous titanium dioxide (TiO₂) at different timescales. We investigate the thermo-optic response of TiO₂ from static regime down to the micro-second regime by applying Joule heating on hybrid metallo-dielectric integrated Mach-Zehnder interferometers. We show that amorphous TiO₂ exhibits a very large negative thermo-optical coefficient in the range of $-6.5 \times 10^{-4} \text{ K}^{-1}$ at 1550 nm at typical timescales of a few seconds. Such a slow thermo-optic response is consistent with an organic origin of amorphous TiO₂ negative thermo-optic coefficient. However, when observed at the micro-second timescale, we show that the same amorphous TiO₂ has a positive thermo-optic coefficient, just like many other materials. Based on our results, TiO₂ can be conveniently deployed in energy-effective integrated optic devices by taking into account the specific multi-timescale thermo-optic properties of this material.

© 2023 Optica Publishing Group under the terms of the [Optica Open Access Publishing Agreement](#)

1. Introduction

Titanium dioxide (TiO₂) is used in optics for decades for free-space optical components coating [1] and more recently in the context of integrated optics [2–6]. Owing to its very broad range of transparency, TiO₂ can be deployed in monolithic visible and infrared photonic devices. TiO₂ can be deposited in many different ways including chemical vapor deposition [7–9], sputtering [10,11], electron-beam evaporation [12,13], atomic layer deposition [14–18] or sol-gel solutions [19]. Depending on the deposition process, TiO₂ layers with refractive index ranging from 1.9 to 2.5 at telecommunication frequencies are obtained. Amorphous TiO₂ are most often of low refractive index whereas anatase and rutile poly-crystalline phases are of intermediate and high refractive index respectively. A very common application of TiO₂ in the field of integrated optics is thermo-optic (TO) control [20–23]. Indeed TiO₂ is known to feature a negative thermo-optic coefficient (TOC) convenient for the fabrication of temperature insensitive integrated devices by compensating for the positive TOC of silicon based waveguiding materials [24–28]. TiO₂ TOC values can be found in the literature ranging from $-0.5 \times 10^{-4} \text{ K}^{-1}$ [21] up to $-4.0 \times 10^{-4} \text{ K}^{-1}$ [13] with TO properties depending very much, not only on the crystalline phase, but also on the temperature range of interest. The reason for such a broad range of TOC values remains unclear given that the rather unusual negative TOC of TiO₂ is attributed to different origins such as thermal expansion or "organic" contributions.

In this work, we investigate TO properties of electron-beam evaporated amorphous TiO₂ at different timescales from second to micro-seconds. Specifically, we show that TiO₂ TOC is

indeed highly negative in the static or quasi-static regime as already reported in many studies but turns to be positive if characterized at the micro-second scale. Our results provide a strong support to the "organic" origin of the negative TOC of TiO₂ whereas at the micro-second scale TiO₂ behaves like many other materials with a positive TOC. The study is organized as follows: we first report on material fabrication and characterizations. Then, we investigate very slow TiO₂ TO properties by spectroscopic ellipsometry (SE). The ellipsometric results are cross-checked by monitoring the TO response of a TiO₂ Mach-Zehnder interferometer (MZI) heated by a Peltier module. Next, we implement a specific metallo-dielectric hybrid waveguiding configuration for optimum joule heating activation of integrated MZI at frequencies ranging from 0.1Hz to several kHz. Based on our observations at different frequencies, we establish that our TiO₂ TOC is of opposite sign in the Hz and kHz regime. Our experimental results are supported by a qualitative analysis relying on the TO response of a 2x2 port MZI. A comprehensive summary of our results and concluding remarks are given in the last section.

2. TiO₂ layer deposition and characterizations

The deposition of our TiO₂ layers is achieved by electron-beam (e-beam) evaporation of 99.99% pure rutile TiO₂ pellets (typical size 3-6 mm). More details about our deposition process are given in Supplemental Materials. Layers with a typical thickness ranging from 200 to 450 nm are investigated in this work. Scanning Electron Microscopy (SEM) images of the layers (see Fig. 1(a)) reveal a compact material with a typical Root Mean Square surface roughness measured by atomic force microscope below 1.5 nm when deposited on a bare silicon substrate. X-Rays Diffraction analysis of our layers (Fig. 1(b)) indicate that room temperature e-beam deposited titanium dioxide is amorphous whereas a deposition temperature increased to 400°C leads to an anatase crystalline phase. X-Rays Photoelectron Spectroscopy (XPS) analysis (Fig. 1(c)) show that our amorphous TiO₂ is stoichiometric. By continuously etching the layer during XPS analysis, we observe the typical carbon contamination at the very surface of the layer whereas this carbon content drops at an atomic fraction below 2% throughout the thickness of the layers.

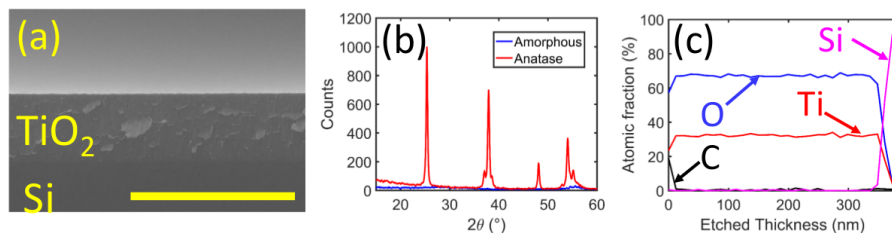


Fig. 1. (a) Scanning Electron Microscope image of an amorphous e-gun deposited amorphous TiO₂ layer on a silicon substrate (scale bar 1 μm). (b) X-Rays Diffraction spectra for amorphous and anatase TiO₂ layers. (c) X-Rays Photoelectron Spectroscopy analysis of an amorphous TiO₂ layer.

3. Thermo-optical characterizations in the static regime

In this section, we discuss thermo-optic (TO) properties of TiO₂ at a time scale of several minutes referenced in the following as the static regime.

3.1. Temperature resolved spectroscopic ellipsometry

TO properties of TiO₂ layers deposited onto bare silicon substrates are first characterized by spectroscopic ellipsometer (WOOLLAM VASE) equipped with a heating cell (Linkam). From SE spectra recorded at thermal equilibrium, the dispersion curves of the purely real refractive

index of a 435 nm-thick TiO₂ layer measured at temperatures of 25°C, 75°C and 125°C are obtained (Fig. 2(a)). Details about SE spectra fitting procedures are given in Supplemental Materials. For an increasing temperature, a very pronounced decrease of the refractive index corresponding to a very large negative TOC is observed. For instance, at a free-space wavelength of $\lambda_0 = 1550$ nm, the refractive index drops from 2.14 at room temperature down to 2.08 at 125°C. In addition, the TOC depends dramatically on the temperature range of interest (see Fig. 2(b)). For example, at 1550 nm, we obtain a TOC of $\frac{dn}{dT} = -6.5 \times 10^{-4} \text{ K}^{-1}$ and $-4.8 \times 10^{-4} \text{ K}^{-1}$ if computed from 25°C-75°C or from 75°C-125°C range respectively. The same trend is reported in the near-infrared (1040nm) in Ref. [13] for e-beam deposited TiO₂ and temperatures above 120°C.

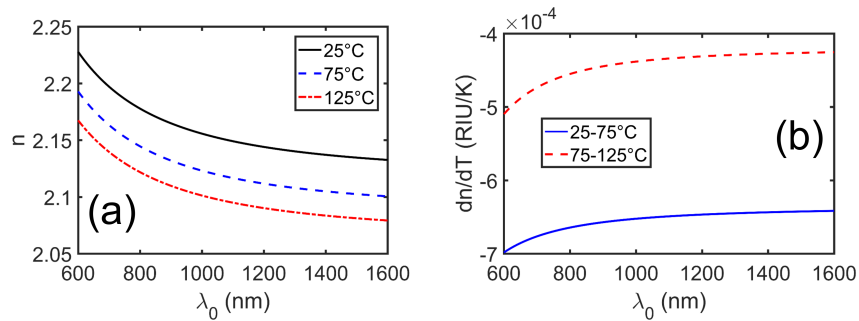


Fig. 2. (a) Dispersion of the purely real refractive index of an amorphous 400 nm-thick amorphous TiO₂. (b) Thermo-Optic coefficient (TOC) dispersion as a function of the temperature range.

Figure 3(a) shows the refractive index at $\lambda_0 = 1550$ nm extracted from SE characterizations of TiO₂ layers submitted to subsequent heating cycles. For the first cycle, the temperature is increased by 50°C step from room temperature (25°C) to 125°C. As expected from the results of Fig. 2, TiO₂ TOC is highly negative but tends to decrease in amplitude as the temperature increases. After the SE spectra was recorded at 125°C, the sample was cooled down to room temperature (in about 1 hour) prior to second cycle. For the heating phase of the second cycle up to 125°C, the refractive index almost superimposes values obtained during the first cycle indicating that TO properties of the layer are not affected by the first heating cycle. At the temperature of 125°C of the second cycle, the temperature was increased up to 300°C. Over this temperature range, it is obvious that the TiO₂ TOC changes in sign resulting in an increase of the refractive index for an increase of the temperature. SE measurements performed during the cooling phase of the sample indicate that the 300°C-baked TiO₂ layers feature a larger refractive index as compared to amorphous TiO₂ whatever the temperature of interest. After overnight cooling, the sample was once again heated up to 125°C during a third cycle. It is apparent that the refractive index of TiO₂ has been permanently affected. XRD characterizations show that the crystalline phase of such high temperature (300°C) baked TiO₂ layers has turned to anatase. As shown in Fig. 3(b), the same experiment repeated onto another layer leads to the same qualitative result with in particular a very clear increase of the refractive index between 225°C and 300°C. After complete cooling, a new heating ramp indicates that the TOC of the polycrystalline anatase TiO₂ layers is negative whatever the temperature range but with a typical value of the TOC close to $\frac{dn}{dT} = -0.5 \times 10^{-4} \text{ K}^{-1}$ at 1550 nm about an order of magnitude smaller as compared to amorphous TiO₂. The effect of annealing of TiO₂ thin films (or other transition metal oxide such as ZrO₂ or Ta₂O₅) optical properties are known and have been reported in the literature for amorphous TiO₂ sol-gel films [29,30] or physical vapor deposited films [31]. When annealed at a sufficient temperature and for a sufficient amount of time (the acquisition of each

data points in Fig. 3(a) and (b) lasts 2 hours), the crystalline phase changes and/or the porosity of the material is reduced leading to a corresponding increase of its refractive index. This process is responsible for the apparent positive ToC for our TiO₂ films when annealed at temperatures above 225-250°C. However, this positive ToC is only characteristic of the phase change. Once the crystalline phase change is completed, the TOC measured in the static regime is negative whatever the temperature range.

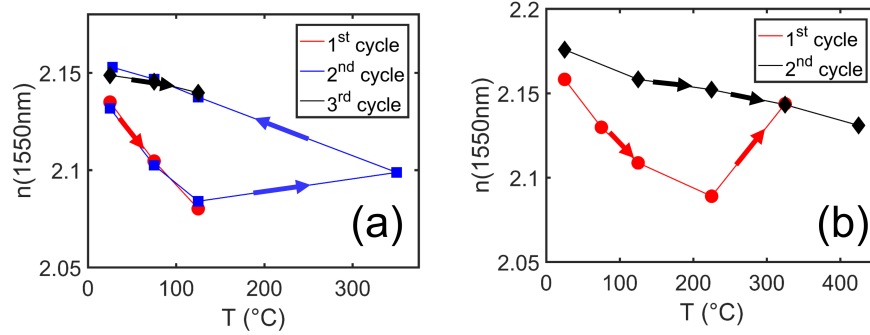


Fig. 3. (a) Temperature dependent refractive index ($\lambda_0 = 1550$ nm) of a 435 nm-thick amorphous TiO₂ during subsequent heating cycles. (b) Same as (a) for a 420 nm-thick amorphous TiO₂ layer.

3.2. Integrated-optics static TO characterizations

In order to confirm SE results, we operate the optical set-up shown in Fig. 4(a) to monitor the transmission of TiO₂ waveguide MZIs (Fig. 4 (b) and (c)) heated in the static regime by a Peltier module. Details about the experimental configuration and the electron-beam lithography fabrication process of the samples are given in Supplemental Materials. We consider a 2×2 MZI with one arm elongated by ΔL compared to the other. The input grating coupler being excited by a transverse electric (TE) incident light at 1550 nm, we monitor the output power at the BAR port of the MZI as a function of temperature. In this experiment, the temperature is measured at the surface of the sample by means of a micro-thermocouple (wires diameter of 100 μ m) glued at the sample surface using a small amount of thermal grease. Owing to MZI arm length difference ΔL , a change ΔT of temperature results in a dephasing between MZI arms given of $\Phi = (n_{eff}(T_0) + \frac{dn_{eff}}{dT} \times \Delta T)k_0\Delta L$ with k_0 the free-space wavevector, $n_{eff}(T_0)$ the effective index of the TE mode at room temperature and $\frac{dn_{eff}}{dT}$ the modal thermo-optic coefficient. Figures 4(c) and (d) show the BAR signal for stretched MZIs with $\Delta L = 167\mu$ m and $\Delta L = 217\mu$ m respectively. The experimental normalized optical transmission data points are fitted with the output signal model at MZI BAR port given by:

$$P_{bar} = P_{in}(\mathcal{R}^2 + \mathcal{T}^2 - 2\mathcal{R}\mathcal{T} \cos \Phi) \quad (1)$$

where \mathcal{R} and \mathcal{T} are 2×2 couplers power reflection and transmission coefficients respectively. The fitting procedure applied to experimental data of Figs. 4(c) and (d) returns a modal TOC of $\frac{dn_{eff}}{dT} = -(5.6 \pm 0.5) \times 10^{-4} \text{ K}^{-1}$ and $\frac{dn_{eff}}{dT} = -(4.8 \pm 0.5) \times 10^{-4} \text{ K}^{-1}$ respectively with the error on the modal TOC estimated from the 95% confidence bounds of the fitting procedure. The modal TOC differs from guiding material TOC by the fact that only a fraction of the modal power is guided within TiO₂. The modal TOC of the photonic mode can be approximated by:

$$\frac{dn_{eff}}{dT} = \eta_{TiO_2} \frac{dn_{TiO_2}}{dT} + \eta_{SiO_2} \frac{dn_{SiO_2}}{dT} \quad (2)$$

where $\eta_{\text{TiO}_2/\text{SiO}_2}$ denotes the modal power confinement of the mode in each material and where $\frac{dn_{\text{TiO}_2/\text{SiO}_2}}{dT}$ is the corresponding material TOC. The contribution of thermally grown SiO_2 can be safely neglected here given its low TOC at 1550nm ($\frac{dn_{\text{SiO}_2}}{dT}=0.09\times 10^{-4}\text{ K}^{-1}$ [32]). The confinement factor of the TE mode supported by our TiO_2 waveguides being evaluated (by finite-element modal analysis) at $\eta_{\text{TiO}_2}=0.78$ (effective index 1.747), we conclude that the TOCs corresponding to Figs. 4(c) and (d) are $\frac{dn_{\text{TiO}_2}}{dT}=-(7.2\pm 0.7)\times 10^{-4}\text{ K}^{-1}$ and $\frac{dn_{\text{TiO}_2}}{dT}=-(6.2\pm 0.7)\times 10^{-4}\text{ K}^{-1}$ respectively in reasonable agreement with the value of $-6.5\times 10^{-4}\text{ K}^{-1}$ returned by SE characterizations over the same temperature range.

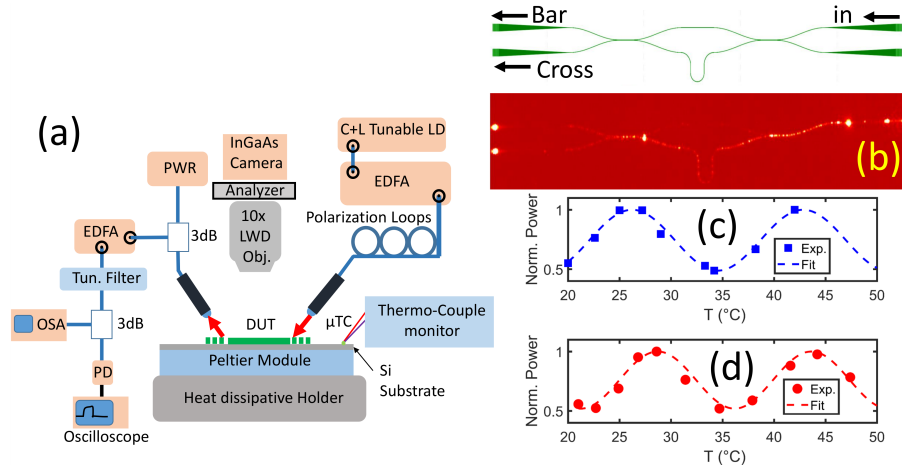


Fig. 4. (a) Optical characterization set-up.(b) Diagrammatic view of the stretched-arm MZI and Infrared image of light ($\lambda_0=1550\text{ nm}$) propagation along the TiO_2 -based stretched-arm MZI. (c) (resp. (d)) Stretched-MZI BAR output transmission as a function of temperature for a difference in length of MZI arms of $\Delta L=167\text{ }\mu\text{m}$ (resp. $\Delta L=217\text{ }\mu\text{m}$).

4. Thermo-optical characterizations at micro-second time scale

4.1. Hybrid metallo-dielectric configuration for TO electrical activation

When using a heating cell or a Peltier module, only very slow TO process can be captured given that these devices allow only for slow changes of temperature (at the scale of tenths of seconds). For TO properties characterizations at micro-second time scale, we implement heaters directly deposited on top of TiO_2 waveguides. The hybrid metallo-dielectric configuration is schematically shown in Fig. 5(a). It is comprised of a TiO_2 ridge waveguide covered with gold heaters. At 1550 nm, the metallo-dielectric hybrid waveguide with a cross-section $1.2 \times 0.450\text{ }\mu\text{m}^2$ sustains a single transverse-electric (TE) mode (see field distribution in Fig. 5(b)) with an effective index of $n_{\text{eff}}=1.78$ and propagation losses around $0.015\text{ dB}/\mu\text{m}$. The hybrid waveguides are implemented only in the arms of the MZIs otherwise made of purely dielectric TiO_2 waveguides. Gold heaters are electrically connected to copper macro-electrodes (see Fig. 5(c)). A SEM image of the transition from the hybrid waveguide to the purely dielectric waveguide is shown in Fig. 5(d). All MZIs considered in the following are equipped with $100\text{ }\mu\text{m}$ -long heaters featuring a typical electrical resistance of $35\text{ }\Omega$ (measured from a four wires configuration, see Supplemental materials). Heat diffusion simulations relying on a realistic finite-element three-dimensional model indicate that the typical heating and cooling times of TiO_2 waveguides in the metallo-dielectric configuration are around $\tau_H=2.1\text{ }\mu\text{s}$ and $\tau_C=2.4\text{ }\mu\text{s}$ respectively (see Supplemental Materials).

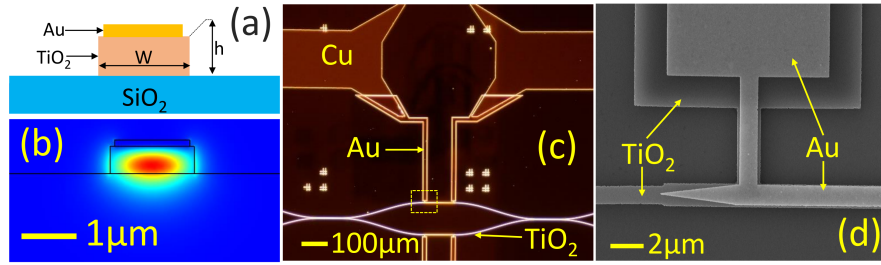


Fig. 5. (a) Cross-section view of the hybrid metallo-dielectric TiO_2 waveguide. (b) Modal intensity distribution of the TE mode supported by the metallo-dielectric waveguide. (c) Dark-field optical microscopy image of a MZI equipped with gold heaters connected to copper macro-electrodes. (d) Scanning electron microscope image of the transition between purely dielectric photonic waveguides and metallo-dielectric waveguides. The SEM image corresponds to the dashed perimeter displayed in (c).

4.2. Quasi-static electrical TO activation

We first consider TO characterizations in the quasi-static regime when a 0.1Hz square voltage is applied to heaters. Figure 6(a) show the applied voltage and the corresponding optical signal for two values of heating (peak) power given by $P_{pk} = R_H \times (\frac{V(t)}{R_E})^2$ with R_H the resistance of the heater, R_E the total resistance of the electrodes and $V(t)$ the time dependent applied voltage. The optical signal is this time observed at the CROSS port of the MZI. When heated with a power of 3.4mW and 4.2mW, the output MZI cross signal drops by about 4.5dB and 14.5dB respectively. This suggests a quite large TOC but neither the sign nor the value of the TOC can be directly extracted from such an experiment since the actual phase difference between the two MZI arms is unknown. Nevertheless, we learn from this experiment that our TiO_2 features a typical TO response time of the order of a few seconds. As shown in Fig. 6(b), the optical signal stabilizes during the heating and cooling phase after roughly 3 seconds. The optical power at the output cross port of a MZI is given by:

$$P_{\text{cross}} = 2P_{\text{in}}\mathcal{R}\mathcal{T}(1 + \cos \Phi) \quad (3)$$

where P_{in} is the input optical power, \mathcal{T} and \mathcal{R} are again transmission and reflection coefficients of the (assumed identical) input and output 2×2 couplers ($\mathcal{R} = \mathcal{T} = 0.5$ for 3dB couplers) and where $\Phi(t)$ is the time dependent phase difference between the two MZI arms. It is noticeable that our experimental results are fairly well fitted by a phenomenological model with a time dependent phase difference given by a single exponential law $\Phi_H(t) = \Phi_0 + \Delta\Phi[1 - \exp(-t/t_H^{DC})]$ during the heating phase and a multi-exponential law $\Phi_C(t) = \Phi_0 + \Delta\Phi[1 - \exp(-t/t_C^{DC})]^2$ during the cooling phase with respective time constants $t_H^{DC} = 1.24\text{s}$ and $t_C^{DC} = 0.95\text{s}$. Thus, the time constants we find for quasi-static excitation are of the order of one second, up to six orders of magnitude larger than heat diffusion time through the cross-section of our metallo-dielectric waveguide. Such a slow response time cannot be attributed to a thermal cross-talk between the $100 \mu\text{m}$ separated MZI arms for two reasons. First, such a cross-talk is not expected from numerical results. Second, by placing the heating electrode one micron aside from TiO_2 waveguide (instead of on top), we observe a dramatic decrease of the quasi-static TO response of our hybrid-MZIs. This dramatic decrease indicates that heat diffusion at the scale of one micron does not allow for a significant heating of the nearby MZI arm thus ruling out the hypothesis of an unintentional heating of the cold MZI arm located $100 \mu\text{m}$ away from the heat source. In summary, quasi-static characterizations indicate that TiO_2 features slow TO response time in the range of a few seconds that cannot be confused with a long-distance heat diffusion process. Finally, we emphasize that the results of this quasi-static experiment cannot be interpreted in terms of annealing-induced

TiO₂ crystalline phase change. Indeed, the optical signal returns to its initial value when the heating source is turned off, demonstrating unambiguously the reversible nature of the process leading to optical signal modulation in Fig. 6(a).

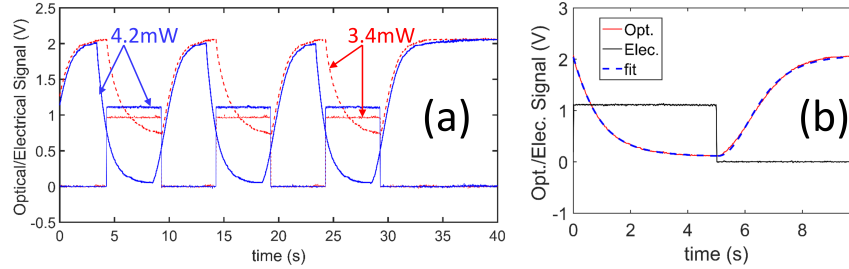


Fig. 6. (a) Simultaneously recorded quasi-static (0.1Hz) electrical pulse voltage and optical CROSS port output signal for peak-power activation of 3.4 and 4.2 mW. (b) For 4.2mW activation peak power, detail over one period of the optical signal along with an empirical model fitting leading to typical time constants around one second heating and cooling phases.

4.3. Pulsed TO activation at kHz frequencies

We consider now TO electrical activation in the kHz frequency regime. Figure 7(a) shows the optical signal recorded at CROSS and BAR output ports of the hybrid-MZI when one electrode of the MZI is activated using electrical pulses with a duration $\tau=10\mu\text{s}$ and a repetition rate of 2.5 kHz (period $400\mu\text{s}$, duty cycle of $dtc=2.5\%$). For electrical pulses of peak power $P_{pk}=33\text{mW}$ (average power $P_{av}=dtc \times P_{pk}=0.82\text{mW}$), we observe in Fig. 7(a) modulated CROSS and BAR output signals of opposite contrast as expected from Eqs. (1) and (3). The experimental CROSS signal is well fitted by Eq. (3) assuming a time dependence of the dephasing given by a single exponential function with time constants $\tau_C=2.5\mu\text{s}$ and $\tau_H=2.1\mu\text{s}$ for heating and cooling phase respectively, in fairly good agreement with heat diffusion time constants returned by numerical calculations. Whatever the output port, the optical signal returns at its baseline value within a few microseconds after the electrical pulse voltage drops to its low state (0V). In the following, we denote this baseline level as the OFF optical signal P^{OFF} (see Fig. 7(a)) because it is observed when the voltage pulse is in low state and corresponds approximately to the average optical signal (DC level) for small duty-cycle excitation pulses. Note however that, P^{OFF} which is observed with voltage pulses applied to the heaters is different from the cool state optical level measured when the MZI is at room temperature with no electrical excitation of the heaters. The electrical excitation of a second MZI at 2.5 kHz generates the output signals displayed in Fig. 7(b) for different pulse duration τ . For increasing τ , the OFF optical signal increases (from almost 0V at $10\mu\text{s}$ up to 1.15V at $15\mu\text{s}$) and the amplitude of the negative contrast CROSS optical pulse increases as well. A typical time of a few seconds is needed for the OFF optical signal to stabilize after τ is changed. Oscilloscope traces exemplifying the stabilization of P^{OFF} are discussed in Supplemental materials. Not only those traces demonstrate the stabilization of P^{OFF} but they also show that the optical signal returns to the room temperature level after pulsed excitation is turned off, indicating that the optical properties of TiO₂ are not permanently affected by the kHz repetition rate short pulses heating we consider in this work. A qualitative interpretation of the results displayed in Fig. 7(b) is the following: at a given frequency, changing τ results in an increase of the average heating power and hence a corresponding increase of the MZI hot arm average temperature T_{av} . The average temperature increases owing to the fact that after each electrical pulse, the hot arm does not fully return at room temperature leading to a slow increase of its temperature with a characteristic time that depends (among many other parameters) on τ and the frequency of the electrical pulses. At a given frequency, T_{av} increases with τ ($\frac{\partial T_{av}}{\partial \tau} > 0$).

For a fixed value of τ , T_{av} eventually saturates when heat dissipation arising from convective processes (with an efficiency that linearly depends on hot arm temperature and thus on T_{av}) entirely dissipate Joule power deposited by each pulse. In the following, we shall refer to the regime corresponding to a stabilized hot arm average temperature as the "stabilized regime" of the MZI (characterized by the time derivative of T_{av} to be zero). In the stabilized regime, the phase difference between MZI arms can be noted:

$$\Phi = \Phi_0 + \Phi_{av}(T_{av}) + \psi(T) \quad (4)$$

where Φ_0 is the phase bias at room temperature, Φ_{av} is the constant additional phase change resulting from the increase of MZI hot arm stabilized average temperature T_{av} and $\psi(T)$ is the dephasing with T the actual temperature of the hot arm at the timescale of a single pulse. In the stabilized regime, the MZI operates at the set-point $\Phi_{sp} = \Phi_0 + \Phi_{av}$ and the optical output is modulated in time by the phase shift $\psi(T)$. If $\psi(T)=0$, the output signal is equal to the OFF optical signal defined above. From Eq. (3), the partial derivative of the output power P_{cross} with respect to time t is given by:

$$\frac{\partial P_{cross}}{\partial t} = -2P_{in}\mathcal{RT} \sin(\Phi) \frac{\partial \psi}{\partial T} \frac{\partial T}{\partial t} \quad (5)$$

Similarly, the partial derivative of the OFF optical signal P_{cross}^{OFF} with respect to T_{av} can be expressed as:

$$\frac{\partial P_{cross}^{OFF}}{\partial T_{av}} = -2P_{in}\mathcal{RT} \sin(\Phi_{sp}) \frac{\partial \Phi_{av}}{\partial T_{av}} \quad (6)$$

For a given τ in Fig. 7(b), P_{cross} monotonously decreases during the heating phase (starting at $t=0\mu s$) and monotonously increases during the cooling phase (starting at $t=\tau\mu s$). The heating (resp. cooling) phase being such that $\frac{\partial T}{\partial t} > 0$ (resp. $\frac{\partial T}{\partial t} < 0$) we conclude that for any values of τ in Fig. 7(b), the factor $-\sin\Phi \frac{\partial \psi}{\partial T}$ in Eq. (5) is negative. In addition, P_{cross}^{OFF} increasing monotonously with τ , the factor $-\sin(\Phi_{sp}) \frac{\partial \Phi_{av}}{\partial T_{av}}$ in Eq. (6) is positive for any τ in Fig. 7(b). Dephasing Φ at $t=0\mu s$ (beginning of the heating pulse) and Φ_{sp} being equal, the sign of $\sin(\Phi)$ and $\sin(\Phi_{sp})$ are necessarily identical and unchanged for any τ in Fig. 7(b) in order for the monotonous change of P_{cross}^{OFF} and P_{cross} to be observed. Hence, based on the above analysis, we conclude that the $\frac{\partial \Phi_{av}}{\partial T_{av}}$ and $\frac{\partial \psi}{\partial T}$ are necessarily of opposite sign.

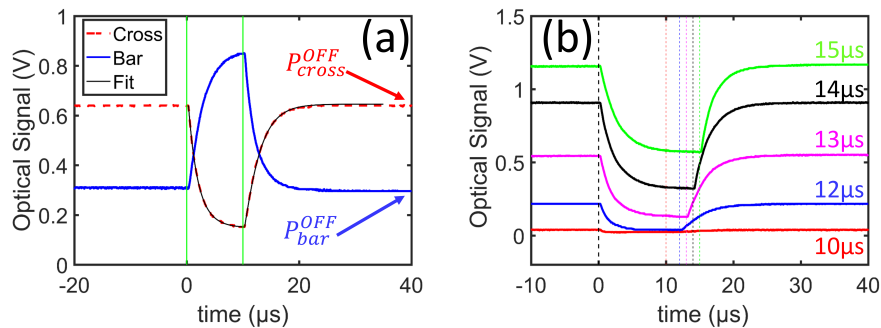


Fig. 7. (a) Comparison of optical cross and bar output signal in case of pulsed TO activation of the MZI at a frequency of 2.5kHz with $10\mu s$ -long pulses at peak power of 33mW. (b) Monitoring of a MZI cross optical signal for pulses of same peak power but increasing duration.

Figure 8(a) shows the change of DC optical signal at the CROSS output port when $\tau=10\mu s$ long pulses (frequency 2.5 kHz) of increasing peak power are applied on one heating electrode.

The DC signal is obtained directly from a powermeter acting as a low-pass filter (cutoff frequency around 100Hz). Owing to the small duty cycle of the pulse, the DC optical signal differs only little from the so-called OFF optical level. The optical signals recorded at various peak powers are displayed in Fig. 8(b). For example, the CROSS optical signal recorded at $P_{pk} = 18.2\text{mW}$ features a positive contrast at the pulse time scale. Increasing P_{pk} to 22.1mW results in a rather flat optical profile and a minimum DC level originating from a phase set-point of the MZI around $\Phi_{sp} = \pi[2\pi]$ rad. Further increasing P_{pk} causes the optical DC signal to increase with the amplitude of the optical pulses increasing as well but this time with a negative contrast. From results of Figs. 8(a) and (b) it is apparent that the slope of optical DC level as a function of the peak power and the contrast of the corresponding optical pulses are of opposite sign. Once again, we emphasize that the DC optical signal stabilizes at the timescale of a few seconds when P_{pk} is changed. Based on the results of Fig. 8(b), we conclude that partial derivatives $\frac{\partial\psi}{\partial T}$ and $\frac{\partial\Phi_{av}}{\partial T_{av}}$ are again of opposite sign with the change of T_{av} caused by the increase of the electrical pulses peak power. The opposite sign of partial derivatives $\frac{\partial\psi}{\partial T}$ and $\frac{\partial\Phi_{av}}{\partial T_{av}}$ is a key result demonstrating that e-beam deposited amorphous TiO_2 features TOCs of opposite sign depending on the timescale.

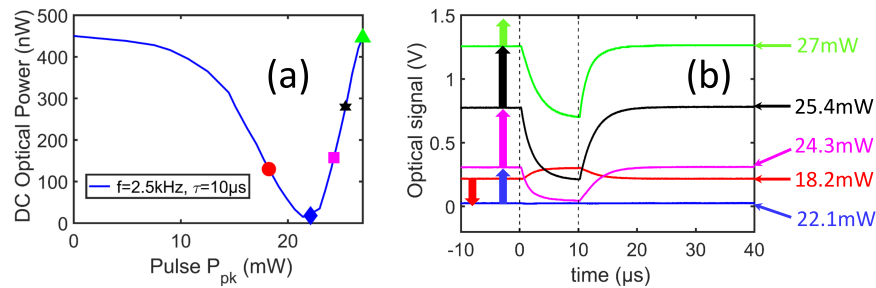


Fig. 8. (A) DC optical signal at the cross port for 2.5kHz pulse with a fixed duration ($10\mu\text{s}$) and increased peak-power. (b) Optical pulses recorded for increasing peak-powers. For each peak-power, the DC optical signal is displayed in (a) with a dot of same face color as the corresponding optical signal.

5. Discussion

TO dynamics of our amorphous TiO_2 can be described as follows: in the static regime (time scale of several minutes), TiO_2 exhibits a large negative TOC. This negative TOC tends to decrease with the heating temperature and can even be affected in a non-reversible way if the heating temperature overcomes a typical value of around 250°C . The non-reversible change of TOC is attributed to a transformation of the crystalline structure of TiO_2 from amorphous to dominantly anatase as shown by XRD experiments. However, when the heating temperature remains below a typical temperature of $125\text{-}150^\circ\text{C}$, the large negative TOC is preserved. Next, in the quasi-static heating regime (time scale of a few seconds), we observe a typical TO response time in the range of 2-3 seconds. Finally, for few micro-second long heat pulses with kHz repetition rate, the optical signal at the MZI output features a slow TO response affecting the average optical level with a contrast in the opposite direction to the optical response observed at the micro-second timescale. Based on this last observation, the TOC of amorphous TiO_2 can be expressed as the sum of a "slow" (second scale) and "fast" (micro-second scale) contributions of opposite sign:

$$\frac{dn_{\text{TiO}_2}}{dT} = \left. \frac{dn_{\text{TiO}_2}}{dT} \right)_{\text{slow}} + \left. \frac{dn_{\text{TiO}_2}}{dT} \right)_{\text{fast}} \quad (7)$$

In static regime, note that both slow and fast TOCs contribute to the TO response. Given that we observe an overall negative TOC in the static regime, it is clear that the slow contribution is

negative and dominates over the fast contribution. The negative TOC of TiO₂ in the static or quasi-static regime has been recognized by several authors and originates very likely from water desorption not only for e-beam evaporated TiO₂ [12] but also for atomic layer deposited material [15,16]. The "organic" origin of amorphous TiO₂ large negative TOC is indeed consistent with the slow (second-scale) TO response time we observe in the quasi-static regime and thus rule out material expansion as the primary cause of such a large negative TOC. Such an "organic" origin of a large negative TOC is also identified in case of lead halide perovskite [33]. In addition, unlike what is commonly admitted for TiO₂, we find that amorphous TiO₂ features a positive TOC at the timescale corresponding to heat diffusion, just like many standard TO materials with a physical origin commonly attributed to a temperature dependent material polarizability.

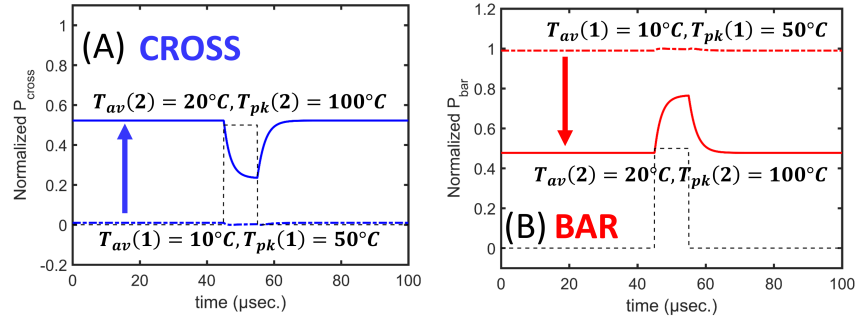


Fig. 9. (A) (resp. (B)) Computed MZI cross (resp. bar) signal in a cold state (1) and a hot state (2) assuming a TOC of the material with a large negative slow contribution ($-3.5 \times 10^{-4} \text{ K}^{-1}$) and a small positive fast contribution of $0.15 \times 10^{-4} \text{ K}^{-1}$. In each figure, the dashed line corresponds to the cold state whereas the solid line is the hot state.

The contrast of the optical signals we consider depends on the MZI output port (CROSS or BAR) and on the unknown phase bias at room temperature. Hence, the analysis of the respective signal contrast can be cumbersome. In this context, it is useful to verify that the interpretation of our experimental results is in qualitative agreement with a simple MZI model. Figure 9(A)(resp. (B)) shows the computed CROSS (resp. BAR) MZI signal computed from transfer function (3) (resp.(1)). In this model, we assume a dephasing between MZI arms given by:

$$\Phi(t) = \Phi_0 + k_0 L_e \left[\left(\frac{dn}{dT} \right)_{slow} \times T_{av} + \left(\frac{dn}{dT} \right)_{fast} \times T_{pk}(t) \right] \quad (8)$$

with k_0 the free-space wavevector, L_e the length of heating electrodes and $\left(\frac{dn}{dT} \right)_{slow/fast}$ referring to modal TOCs of the hybrid metallo-dielectric waveguide. Temperatures T_{av} corresponds to the stabilized average temperature during a pulsed heating of the MZI and T_{pk} is the amplitude of the temperature change at the time scale of one heating pulse. In Figs. 9(A) and (B), optical profiles are obtained for the phase bias $\Phi_0 = -2\pi/3$ rad. and temperatures set for cold and hot states. The output signals are computed assuming $\left(\frac{dn}{dT} \right)_{slow} = -3.5 \times 10^{-4} \text{ K}^{-1}$ and $\left(\frac{dn}{dT} \right)_{fast} = +0.15 \times 10^{-4} \text{ K}^{-1}$. By using opposite signs fast and slow TOCs, we observe a behavior of the CROSS signal (Fig. 9(A)) in full qualitative agreement with the experimental profiles displayed in Fig. 8(b) with in particular an increase of the OFF level and the corresponding development of a negative contrast pulse. A similar inverted contrast is observed for BAR signal in Fig. 9(B) (decrease of OFF level and positive contrast pulse). The change of average level and the corresponding pulse contrast is obviously dependent on the choice of the phase set-point Φ_0 meaning that depending Φ_0 the results for CROSS and BAR signals could be reversed. Nonetheless, whatever Φ_0 or

output ports, an optical pulse with a contrast reversed compared to the change of the average optical signal is indicative of opposite sign TOCs at short and long timescales.

6. Conclusion

In summary, we have investigated the dynamics of thermo-optical properties of amorphous e-beam deposited titanium dioxide. By operating different optical characterization techniques at different timescales, we show that e-beam deposited TiO₂ features a large negative TOC with a typical response in the range of one second. This large negative TOC depends on the crystalline phase of the material and is found to decrease with an increasing temperature range used for the measurement of the TOC. Such a behavior suggests an organic origin of this large negative TOC in agreement with the conclusion of previous studies. However, when observed at the timescale of micro-second (corresponding to typical time constants of heat diffusion process through our integrated waveguides), we note that the TOC of our amorphous TiO₂ is of opposite sign as compared to the slow TO response. At this timescale, the amorphous TiO₂ TOC is positive similarly to many other TO materials with a physical origin of this property related to the material polarisability. Our results lead to several important conclusions. First, from a practical point of view, owing to its large negative static TOC, amorphous TiO₂ can be operated in TO devices for energy efficient phase set-point adjustment with the limitation that the organic origin of static TO properties could be source of instabilities. Second, our results illustrate the importance of multi-timescales optical characterizations for the determination of material TO properties in particular for materials with a negative TOC. Indeed, if a TO material exhibits short and long timescale TO response, standard static characterizations techniques such as spectroscopic ellipsometry or Peltier module activated integrated optics configurations pick-up the sum of the slow and fast contributions to the TO response. Hence, based solely on the results of such static techniques, one can erroneously conclude that a material has a weak or no TO activity when in fact the slow and fast TO contributions are both large but fully or partially counterbalance each other. Finally, the results we report in this work are for amorphous TiO₂ featuring a quite large negative TOC in the static regime. As a direct continuation of this work, it would be interesting to check whether moderate negative TOC TiO₂ such as anatase crystalline phase TiO₂ exhibits similar multi-timescale thermo-optic properties.

Funding. Horizon 2020 Framework Programme (EU-H2020-871391-PlasmoniAC, EU-H2020-871658-Nebula).

Acknowledgments. The authors acknowledge financial support from H2020-871391 PlasmoniAC and EU-H2020-RIA-ICT-2019-2 Agreement No: 871658 NEBULA projects. This work was carried out using equipment of ARCEM micro-fabrication platform and has received support from the french Renatech+ network. The authors thank Olivier Heinz for XPS analysis and J. Lopez and B. Gourier from "Centre de Ressources Mécaniques" of LICB for their technical support in the design and fabrication of optimized thermally dissipative sample holders.

Disclosures. The authors declare no conflicts of interest.

Data availability. Data underlying the results presented in this paper are not publicly available at this time but may be obtained from the authors upon reasonable request.

Supplemental document. See [Supplement 1](#) for supporting content.

References

1. S. F. Pellicori and H. L. Hettich, "Reversible spectral shift in coatings," *Appl. Opt.* **27**(15), 3061 (1988).
2. J. D. B. Bradley, C. C. Evans, J. T. Choy, O. Reshef, P. B. Deotare, F. Parsy, K. C. Phillips, M. Lončar, and E. Mazur, "Submicrometer-wide amorphous and polycrystalline anatase TiO₂ waveguides for microphotonic devices," *Opt. Express* **20**(21), 23821–23831 (2012).
3. C. C. Evans, C. Liu, and J. Suntivich, "Low-loss titanium dioxide waveguides and resonators using a dielectric lift-off fabrication process," *Opt. Express* **23**(9), 11160–11169 (2015).
4. C. C. Evans, K. Shtyrkova, J. D. B. Bradley, O. Reshef, E. Ippen, and E. Mazur, "Spectral broadening in anatase titanium dioxide waveguides at telecommunication and near-visible wavelengths," *Opt. Express* **21**(15), 18582–18591 (2013).

5. K. Hammani, L. Markey, M. Lamy, B. Kibler, J. Arocas, J. Fatome, A. Dereux, J.-C. Weeber, and C. Finot, "Octave spanning supercontinuum in titanium dioxide waveguides," *Appl. Sci.* **8**(4), 543 (2018).
6. X. Guan, H. Hu, L. K. Oxenløwe, and L. H. Frandsen, "Compact titanium dioxide waveguides with high nonlinearity at telecommunication wavelengths," *Opt. Express* **26**(2), 1055–1063 (2018).
7. S. Wiechmann and J. Müller, "Thermo-Optics properties of TiO₂, Ta₂O₅ and Al₂O₃ thin films for integrated optics on silicon," *Thin Solid Films* **517**(24), 6847–6849 (2009).
8. T. Maekawa, K. Kurosaki, T. Tanaka, and S. Yamanaka, "Thermal conductivity of titanium dioxide films grown by metal-organic chemical vapor deposition," *Surf. Coat. Technol.* **202**(13), 3067–3071 (2008).
9. A. Andrieux, M.-M. Mennemanteuil, N. Geoffroy, M. Eno, L. Markey, and K. Hammani, "Optimized ICPCVD-based TiO₂ for photonics," *Materials* **15**(7), 2578 (2022).
10. Y.-H. Wang, K. H. Rahman, C.-C. Wu, and K. C. Chen, "A review on the pathway of the improved structural characteristics and photocatalytic performance of titanium dioxide (TiO₂) thin films fabricated by magnetron-sputtering technique," *Catalyst* **10**(6), 598 (2020).
11. M. Brella, A. Taabouche, B. Gharbi, R. Gheriani, Y. Bouachiba, A. Bouabellou, H. Serrar, S. Touil, K. Laggoune, and M. Boudissa, "Comparison of thin films of titanium dioxide deposited by sputtering and sol-gel methods for waveguiding applications," *Semiconductors* **56**(3), 234–239 (2022).
12. M. Gilo and N. Croitoru, "Properties of TiO₂ films prepared by ion-assisted deposition using a gridless end-Hall ion source," *Thin Solid Films* **283**(1-2), 84–89 (1996).
13. G. Gülsen and M. Naci Inci, "Thermal optical properties of TiO₂ films," *Opt. Mater.* **18**(4), 373–381 (2002).
14. M. R. Saleem, P. Silfsten, S. Hokanen, and J. Turunen, "Thermal properties of TiO₂ films grown by atomic layer deposition," *Thin Solid Films* **520**(16), 5442–5446 (2012).
15. M. R. Saleem, R. Ali, S. Honkanen, and J. Turunen, "Thermal properties of thin Al₂O₃ films and their barrier layer effect on thermo-optic properties of TiO₂ films grown by atomic layer deposition," *Thin Solid Films* **542**, 257–262 (2013).
16. R. Ali, M. R. Saleem, P. Pääkkönen, and S. Honkanen, "Thermo-optical properties of thin-film TiO₂-Al₂O₃ bilayers fabricated by atomic layer deposition," *Nanomaterials* **5**(2), 792–803 (2015).
17. B. D. Piercy, C. Z. Leng, and M. Losego, "Variation in the density, optical polarizability and crystallinity of TiO₂ thin films deposited via atomic layer deposition from 38°C to 150°C using the titanium tetrachloride-water reaction," *J. Vac. Sci. Technol. A* **35**(3), 03E107 (2017).
18. H. Park, J. Jung, Y. Zhang, M. Liu, J. Lee, H. Noh, M. Choi, S. Lee, and H. Park, "Effect of thermally induced phase transition on the negative thermo-optic properties of Atomic-layer-deposited TiO₂ films," *ACS Appl. Electron. Mater.* **4**(2), 651–662 (2022).
19. Z. Chen, M. Wei, Y. Luo, J. Jian, Y. Ye, Y. Yin, C. Sun, C. Zhong, K. Si, D. Zhang, H. Lin, and L. Li, "Efficient and compact sol-gel TiO₂ thermo-optic microring modulator," *Opt. Mater. Express* **12**(10), 4061–4071 (2022).
20. J. Park, S. K. Ozdemir, F. Monifi, T. Chadha, S. He Huang, P. Biswas, and L. Yang, "Titanium dioxide whispering gallery microcavities," *Adv. Opt. Mater.* **2**(8), 711–717 (2014).
21. O. Reshef, K. Shryrkova, M. G. Moebius, S. Griesse-Nascimento, S. Spector, C. C. Evans, E. Ippen, and E. Mazur, "Polycrystalline anatase titanium dioxide microring resonators with negative thermo-optic coefficient," *J. Opt. Soc. Am. B* **32**(11), 2288–2293 (2015).
22. H. Yu and F. Qiu, "Compact thermo-optic modulator based on a titanium dioxide micro-ring resonator," *Opt. Lett.* **47**(8), 2093–2096 (2022).
23. Z. Chen, M. Wei, B. Sun, Y. Weng, J. Jian, C. Zhong, C. Sun, K. Si, W. Gong, H. Lin, and L. Li, "Flexible waveguide integrated thermo-optic switch based on TiO₂ platform," *Opt. Lett.* **48**(12), 3239–3242 (2023).
24. F. Qiu, A. M. Spring, F. Yu, and S. Yokohama, "Complementary metal-oxide-semiconductor compatible athermal silicon nitride/titanium dioxide hybrid micro-ring resonators," *Appl. Phys. Lett.* **102**(5), 051106 (2013).
25. S. S. Djordevic, K. Shang, B. Guan, S. T. S. Cheung, L. Liao, J. Basak, H.-F. Liu, and S. J. B. Yoo, "CMOS-compatible, athermal silicon ring modulators clad with titanium dioxide," *Opt. Express* **21**(12), 13958–13968 (2013).
26. S. Feng, K. Shang, J. T. Bovington, R. Wu, B. Guan, K.-T. Cheng, J. E. Bowers, and S. J. B. Yoo, "Athermal silicon ring resonators clad with titanium dioxide for 1.3 μm wavelength operation," *Opt. Express* **23**(20), 25653–25660 (2015).
27. F. Qiu, A. M. Spring, and S. Yokoyama, "Athermal and high-Q TiO₂-Si₃N₄ ring resonator via an etching-free fabrication technique," *ACS Photonics* **2**(3), 405–409 (2015).
28. S. Namnabat, K.-J. Kim, A. Jones, R. Himmelhuber, C. T. DeRose, D. C. Trotter, A. L. Starbuck, A. Pomerene, A. L. Lentine, and R. A. Norwood, "Athermal silicon optical add-drop multiplexers based on thermo-optic coefficient tuning of sol-gel material," *Opt. Express* **25**(18), 21471–21482 (2017).
29. N. R. Mathews, E. R. Morales, M. A. Cortés-Jacome, and J. A. Toledo Antonio, "TiO₂ thin films-Influence of annealing temperature on structural optical and photocatalytic properties," *Sol. Energy* **83**(9), 1499–1508 (2009).
30. J. Ben Naceur, M. Gaidi, F. Bousbih, R. Mechiakh, and R. Chtourou, "Annealing effect on microstructural and optical properties of nanostructured-TiO₂ thin films prepared by sol-gel techniques," *Curr. Appl. Phys.* **12**(2), 422–428 (2012).
31. M. M. Hasan, A. S. M. A. Haseeb, R. Saidur, H. H. Masjuki, and M. Hamdi, "Influence of substrate and annealing temperatures on optical properties of RF-sputtered TiO₂ thin films," *Opt. Mater.* **32**(6), 690–695 (2010).

32. F. A. Memon, F. Morichetti, and A. Melloni, "High thermo-optic coefficient of silicon oxycarbide photonic waveguides," *ACS Photonics* **5**(7), 2755–2759 (2018).
33. T. Handa, H. Tahara, T. Aharen, and Y. Kanemitsu, "Large negative thermo-optic coefficients of lead halide perovskite," *Sci. Adv.* **5**(7), eaax0786 (2019).